Analysis and Optimal Design of High Frequency and High Efficiency Asymmetrical Half-Bridge Flyback Converters

Li, Mingxiao; Ouyang, Ziwei; Andersen, Michael A. E.

Published in:
IEEE Transactions on Industrial Electronics

Link to article, DOI:
10.1109/tie.2019.2950845

Publication date:
2020

Document Version
Peer reviewed version

Analysis and Optimal Design of High Frequency and High Efficiency Asymmetrical Half-Bridge Flyback Converters

Mingxiao Li, *Student Member, IEEE,* Ziwei Ouyang, *Senior Member, IEEE*
and Michael A.E. *Andersen*, *Member, IEEE*

***Abstract*—The asymmetrical half-bridge (AHB) flyback converter is capable to achieve zero voltage switching (ZVS) and has lower voltage stress compared to the active clamp flyback converter (ACF). This topology gives much margin for components selection and transformer turns ratio design. It is well adapted to voltage step-down applications. However, the optimal design for AHB flyback converter taking current dip effect causing by components parasitic capacitances, and each component effect to power loss into consideration has never been explored. This paper gives detailed operation and mathematical analyses of this effect. The optimal design procedure with the consideration of each circuit parameter is presented in this paper. The transformer benefits low power loss from interleaving winding layout. A 56W/inch^3 1MHz 65W prototype with 100V-250V input is built to verify the feasibility of the converter. Experimental results show the peak efficiency 96.5% is achieved with 127V input and the whole system efficiency under the entire input voltage range is above 93%.**

***Index Term*— AHB flyback converter, high efficiency, voltage step down applications**

I. Introduction

With the increasing demand for size reduction and high power density, high frequency operation provides a way to achieve these goals. The emerging gallium nitride (GaN) devices open the door for Megahertz (MHz) range switching frequency operation. GaN devices show better performance than silicon MOSFETs under a similar voltage and current ratings, such as smaller output capacitance, lower gate charge and smaller package. Thus GaN devices can be applied to a considerably high frequency converters design [1]-[6].

Among many DC/DC converters, flyback converters have been widely used in many applications, such as switching mode power supplies, adaptors for tablets and smartphones, PV systems, etc. However, traditional flyback converter operating at hard switching mode cannot reach high efficiency at high frequency. Both voltage and current stress are very high due to the energy stored in transformer leakage inductance. The conventional passive clamping method helps reduce the leakage energy by using the clamp resistor. This reduces the switch voltage stress, but the efficiency is not improved. Active clamp flyback converters have been proposed in [6]-[8] to fully utilize the leakage energy to achieve soft-switching. It has been proved to achieve high efficiency at high frequency. Many publications have done excellent works on ACF design [9]-[17]. However, the high voltage stress for ACF is still a problem. It poses obstacles to components selection and transformer design.

The AHB flyback converter has lower voltage stress compared to ACF and is also capable to achieve soft-switching, which is gaining popularity. It can achieve strong output voltage regulation through PWM control, which is the same with ACF. On the other hand, LLC is not suitable to be used in the applications with a wide input voltage range, whose regulation capability relies on the small inductance ratio of magnetizing inductance to resonant inductance. A large resonant inductor is required, leading to small power density and low efficiency. This topology is not considered in this paper.

Many publications have done excellent analyses on AHB flyback converter. It can be regarded as a buck converter with a transformer [18]-[23]. Thus it is well adapted to voltage step-down applications. The switching loss is reduced and a larger margin for components selection and turns ratio design are given. Detailed operating principles can be found in [18][20][22]. The hybrid-switching technique is proposed in [23] to achieve ZVS for primary switches and ZCS for the secondary rectifier. However, ZCS realization relies on the resonance between the resonant inductor and resonant capacitor. It leads to high primary and secondary RMS current. Detailed analysis can be found in this paper. Literature [24] gives conventional analysis and design procedure for AHB flyback converter, but the current dip effect is not considered. It affects primary and secondary RMS current.

To obtain soft-switching properties, capacitances of switches are always taken into consideration, as many publications have explored [19][20][24][25]. However, the current dip effect due to the current shared by the primary and secondary capacitances has never been mentioned or investigated in optimal design procedure for AHB flyback converters. At Mega Hz operation, they are of great importance to design a high performance converter. This paper gives detailed analyses of the current dip effect due to the current shared by the primary and secondary capacitances, which affects both primary and secondary RMS current and further power loss. This effect can be used to select primary and secondary switches. The flux cancellation in the transformer is first mentioned in this paper. The AHB flyback converter benefits low winding loss from interleaving winding layout. Additionally, the impact of the resonant capacitor on primary and secondary RMS current and the optimal magnetizing inductance design with the consideration of power loss are investigated. An optimal design procedure is given and iterations are then conducted to select the turn ratio with minimum power loss. The half-turn winding paralleled concept proposed in [26] is adopted to minimize the transformer AC resistance.

Manuscript received April 10, 2019; revised August 13, 2019 and September 16, 2019; accepted October, 2019. (Corresponding author: Ziwei Ouyang)

The authors are with the Department of Electrical Engineering, Technical University of Denmark, Kgs. Lyngby 2800, Denmark (e-mail: mingxli@elektro.dtu.dk; zo@elektro.dtu.dk;ma@elektro.dtu.dk).

This paper is organized as follows: Section II gives the detailed operating principle and analyses of the current dip effect along with mathematical equations and waveforms. A comparison of the traditional ACF and the AHB flyback converter is also illustrated. The optimal design procedure is described in Section III. A 56W/inch^3 1MHz 65W with peak efficiency 96.5% prototype is demonstrated in Section IV. Section V concludes this paper.

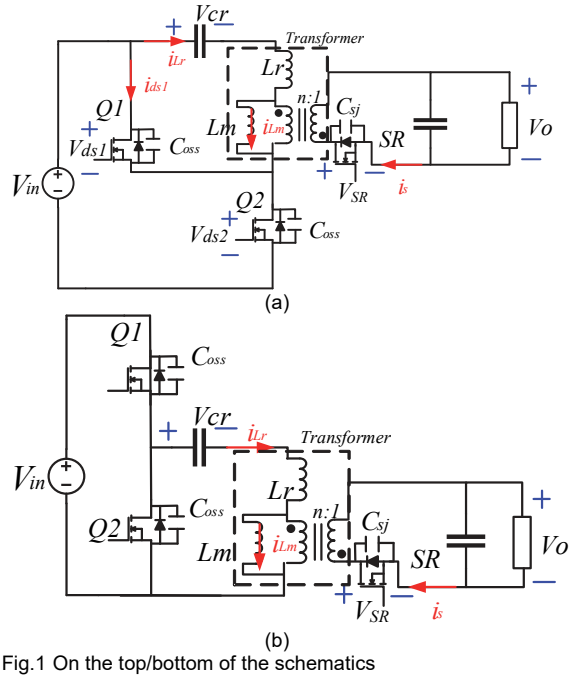

Fig.1 On the top/bottom of the schematics

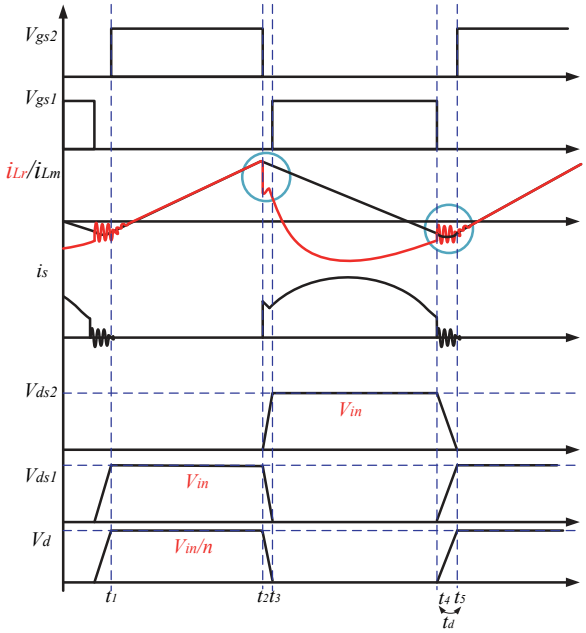

Fig.2 Waveforms of the proposed topology

II. Analyses of the AHB Flyback Converter

Two configurations of the AHB flyback converter are illustrated in Fig.1 (a) and Fig.1 (b), respectively. Q_1 and Q_2 form a half-bridge configuration. The switch node is connected to the transformer and the resonant capacitor. The switch Q_1 toggles complementarily concerning Q_2. Thus the voltage stress on Q_1 and Q_2 is always clamped by the input voltage, regardless of the transformer turns ratio and output voltage. Waveforms of the proposed converter operating close to the CCM/DCM mode boundary is shown in Fig.2. Since the operating principles of these two configurations are identical, only the Fig.1(a) is analyzed. Both steady-state and operating principles analyses of this topology are discussed in this section.

A. Steady-state analyses

To analyze this circuit, the following assumptions are made

—The output voltage V_o is a constant value

—The resonant inductance L_r is much smaller than the magnetizing inductance L_m.

—Conduction power losses of all switches are neglected.

—The resonant capacitor C_r can be taken as a constant voltage source.

—The conduction times for Q_1 and Q_2 are $(1\text{-}D)T_s$ and DTs, respectively, where D is the duty cycle for Q_2 and T_s is the switching period. Dead time is neglect in the steady-state analysis.

Based on the assumptions mentioned above, the voltage transfer ratio V_o/V_{in} and the voltage across the resonant capacitor V_{cr} can be obtained when voltage second balance is applied to magnetizing inductance L_m. When the bottom switch Q_2 turns on, the voltage across the transformer primary winding is V_{in}-V_{cr} and Q_1 is clamped by the input voltage V_{in}. In the next time interval, Q_2 turns off while Q_1 turns on. The voltage applied to the transformer primary winding becomes $-V_{cr}$. Q_2 is clamped by the input voltage V_{in}. Apply voltage second balance on magnetizing inductance and the voltage across the resonant capacitor can be expressed by (1)

$$D\left(V_{in}-V_{Cr}\right)=V_{Cr}\left(1-D\right)$$
$$V_{Cr}=V_{in}D \tag{1}$$

The converter is operating close to the CCM/DCM boundary with the relatively small magnetizing current. It has a negligible effect on (1). The voltage-second-balance law can still be used. The same approximation can be found in [14][24][25].

nV_o is applied to magnetizing inductance during the period when Q_1 is on. If L_r cannot be ignored, V_{cr} should be expressed by

$$V_{Cr}=nV_o\left(1+\frac{L_r}{L_m}\right)$$

Based on the given assumption, L_r is much smaller than the magnetizing inductance L_m. Thus V_{Cr} is very close to the reflected output voltage nV_o. The same approximation can be found in [14][24][25]. The voltage transfer ratio can be found in (2)

$$D\left(V_{in}-V_{Cr}\right)=nV_o\left(1-D\right)$$
$$\frac{V_o}{V_{in}}=\frac{D}{n} \tag{2}$$

Then the voltage across secondary synchronous rectifier (SR) when Q_2 turns on, V_{SR} can be found to be

$$V_{SR}=V_{in}/n \tag{3}$$

TABLE I
COMPARISON BETWEEN TRADITIONAL ACF AND AHB FLYBACK

	V_{ds1}/V_{ds2}	V_{SR}	V_o/V_{in}
ACF	$V_{in}+nV_o$	$V_{in}/n+V_o$	$D/n(1\text{-}D)$
AHB flyback	V_{in}	V_{in}/n	D/n

The comparison between ACF and AHB flyback converter is shown in TABLE I. The voltage stresses for both primary and secondary switches are reduced, which offers much margin to select primary and secondary components and transformer turns ratio. It is also worthwhile to point out that the voltage stress for the primary main switch of ACF is higher than $V_{in}+nV_o$ due to the voltage across the leakage inductance. On the other hand, that for the AHB flyback converter is always clamped by the input voltage V_{in}. This provides a safe selection for primary switches. More importantly, since there is no *1-D* in the denominator of the voltage transfer ratio for the AHB flyback converter, it is more preferable to be used in voltage step down cases. In another word, the traditional ACF converter can be regarded as a buck-boost converter, while the AHB flyback converter functions as a buck converter. Its capability to step the voltage down is higher than the traditional ACF. With all mentioned merits, it is more preferable for voltage step down applications.

B. Operating principles analyses

Stage 1 ($t_1<t<t_2$): Q_2 ZVS turns on at t_1 and then the drain-to-source voltage of Q_1 V_{ds1} is clamped by input voltage $V_{in.}$ The secondary rectifier is blocked. The energy is stored in the transformer. The magnetizing current i_m increases linearly together with the resonant current i_{Lr} and can be expressed by

$$i_{Lr}(t)=i_{Lm}(t)=i_{Lr}(t_1)+\frac{V_{in}-V_{Cr}}{L_r+L_m}t \tag{4}$$

This time interval ends when Q_2 turns off at t_2.

Stage 2 ($t_2<t<t_3$): A current dip happens to the resonant current i_{Lr} during the transient period after Q_2 turns off at time t_2, which can be observed from Fig.2. It affects both primary and secondary RMS current. Detailed analysis of this effect will be given in the following description.

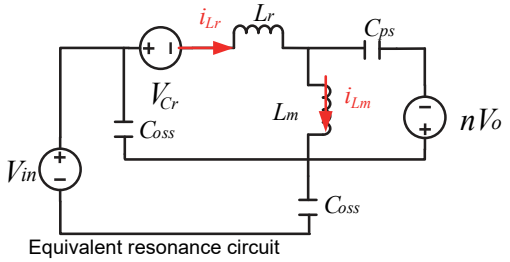

Fig.3 Equivalent resonance circuit

Resonance occurs among L_r, output capacitances C_{oss} of primary switches and secondary rectifier output capacitance C_{sj}. The equivalent circuit is shown in Fig.3. C_{ps} is C_{sj} referred to the primary side. Assume the magnetizing current i_m maintains the peak value I_{Lm_max} during this transient period, which can be calculated by

$$I_{Lm\_max}=I_{Lm\_avg}+\frac{nV_o(1-D)(T_s-t_d)}{2L_m} \tag{5}$$

$$I_{Lm\_avg}=I_{Lr\_avg}+I_{s\_avg}=\frac{I_o}{n} \tag{6}$$

where t_d is the dead time as shown in Fig.2. Only the dead time between t_4 to t_5 is considered because it takes longer time than that from t_2 to t_3 for the small reverse magnetizing current to charge and discharge the parasitic capacitances; I_o is the output current. The average resonant current I_{Lr_avg} is zero when the law of charge balance is applied to the resonant capacitor.

Then the resonant current i_{Lr} can be solved by [14]

$$i_{Lr}(t)\approx I_{Lm\_max}\frac{2C_{oss}}{2C_{oss}+C_{ps}}+I_{Lm\_max}\frac{C_{ps}}{2C_{oss}+C_{ps}}\cos(\omega_r t) \tag{7}$$

where

$$\omega_r=1/\sqrt{\frac{2C_{oss}C_{ps}}{2C_{oss}+C_{ps}}L_r} \tag{8}$$

Due to the large peak magnetizing current I_{Lm_max}, Q_1 is usually fully discharged within one resonance period. The maximum current dip when the resonance is longer than half period can be obtained by

$$I_{dip\_max}=I_{Lm\_max}\frac{2C_{ps}}{2C_{oss}+C_{ps}} \tag{9}$$

Equation (9) illustrates that the resonant current dip is due to the current shared by the primary and secondary capacitances. The maximum current dip is determined by the ratio C_{ps}/C_{oss}.

If the resonance is shorter than the half period, the current dip is lower. Actually, the resonance stops when C_{oss} of Q_1 is fully discharged or C_{sj} of the secondary rectifier is fully discharged. The expressions for V_{ds1} and V_{SR} are given as follows:

$$V_{ds1}(t)=V_{in}-\frac{I_{Lm\_max}t}{2C_{oss}+C_{ps}}-\frac{I_{Lm\_max}C_{ps}}{2C_{oss}+C_{ps}}\cdot\frac{\sin(\omega_r t)}{\omega_r 2C_{oss}} \tag{10}$$

$$nV_{SR}(t)=V_{in}-\frac{I_{Lm\_max}t}{2C_{oss}+C_{ps}}+\frac{I_{Lm\_max}C_{ps}}{2C_{oss}+C_{ps}}\cdot\frac{\sin(\omega_r t)}{\omega_r C_{ps}} \tag{11}$$

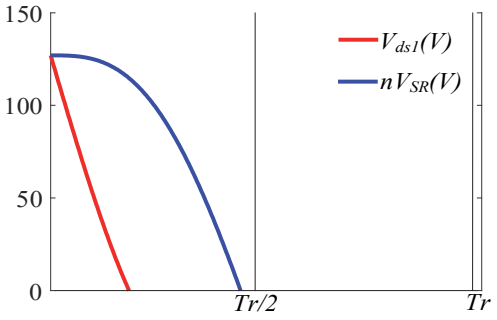

(a)

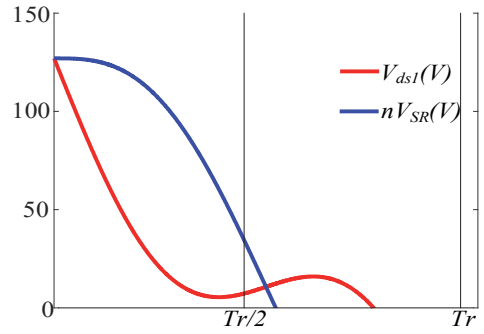

(b)

Fig.4 V_{ds1} and V_{SR} waveforms during ZVS transition period when (a) C_{oss}=8pF and C_{sj}=200pF; (b)C_{oss}=17pF and C_{sj}=400pF

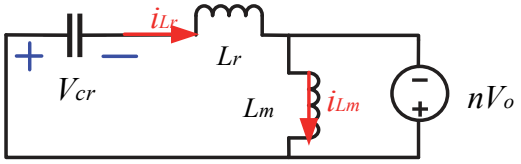

Fig.5 Equivalent circuit of L_r and C_r resonant process

Large C_{oss} and C_{ps} give longer resonance, which is longer than half resonance period. In this case, V_{SR} drops to zero first. By contrast, small C_{oss} and C_{ps} give short resonance, which is shorter than half resonance period and V_{ds1} will drops to zero first. This phenomenon is shown in Fig.4. If the resonance is much smaller than the half resonance period T_r, $sin(\omega_r t)$ can be replaced by $\omega_r t$. V_{ds1} decreases to zero linearly. Thus it will not join in the resonance and the resonance current expressions can be solved by

$$i_{Lr}(t) = I_{Lm\_max} - \frac{\frac{V_{in}-V_{Cr}}{L_m+Lr}L_m + V_{Cr}}{Z_{r1}}\sin(\omega_{r1}t) \quad (12)$$

$$Z_{r1} = \sqrt{L_r / C_{ps}}, \omega_r = 1/\sqrt{L_r C_{ps}} \quad (13)$$

The maximum current dip becomes

$$I_{dip\_max} = \frac{V_{in} + V_{Cr}\frac{L_r}{L_m}}{1 + L_r / L_m}\frac{1}{Z_{r1}} \quad (14)$$

Equation (14) shows when the resonance is less than half resonance period, the ratio of L_r/C_{ps} will affect the maximum current dip. Since the magnetizing inductance L_m is much larger than L_r, I_{dip_max} depends on Z_{r1}.

Stage 3 ($t_3<t<t_4$): After the current dip happens to i_{Lr}, Q_1 and secondary rectifier start to conduct current. Resonance occurs between L_r and C_r. The difference between i_{Lr} and i_{Lm} is transferred to the secondary side. The magnetizing inductance is clamped by nV_o. The resonant process of L_r and C_r is the same with traditional active clamp flyback converter, but the initial conditions are different. The equivalent resonant circuit is shown in Fig.5 and the expressions for magnetizing current i_{Lm} and resonant current i_{Lr} during this time interval are shown as follows

$$i_{Lm}(t) = I_{Lm\_max} - \frac{nVo}{L_m}t \quad (15)$$

$$i_{Lr}(t) = I_{Lr\_ini}\cos(\omega t) + \frac{(nV_o - V_{Cr\_ini})}{Z}\sin(\omega t) \quad (16)$$

$$V_{Cr\_ini} \approx nV_o + \frac{(I_{Lm\_max} + I_{Lm\_min})DT_s}{2C_r} \quad (17)$$

$$I_{Lm\_min} = I_{Lm\_avg} - \frac{nV_o(1-D)(T_s - t_d)}{2L_m} \quad (18)$$

$$\omega = 1/\sqrt{L_r C_r}, Z = \sqrt{\frac{L_r}{C_r}} \quad (19)$$

where V_{Cr_ini} is the initial voltage across the resonant capacitor before the resonance starts and can be estimated based on the charge balance; I_{Lm_min} is the minimum magnetizing current; I_{Lr_ini} is the resonant current after the current dip. It can be expressed by

$$I_{Lr\_ini} = I_{L_m\_\max}\frac{2C_{oss} - C_{ps}}{2C_{oss} + C_{ps}} \quad (20)$$

or

$$I_{Lr\_ini} = I_{Lm\_max} - \frac{\frac{V_{in}-V_{Cr}}{L_m+Lr}L_m + V_{Cr}}{Z_{r1}} \quad (21)$$

depending on the resonance longer or shorter than the half resonance period.

Stage 4 ($t_4<t<t_5$): The current dip also occurs during this ZVS transition period after Q_1 turns off. The equivalent resonant circuit is also the same with the previous ZVS transition period as shown in Fig.3, while the initial conditions are different. The similar expression for resonant current i_{Lr} is shown as follows:

$$i_{Lr}(t) \approx i_{Lr}(t_4)\frac{2C_{oss}}{2C_{oss}+C_{ps}} + i_{Lr}(t_4)\frac{C_{ps}}{2C_{oss}+C_{ps}}\cos(\omega_r t) \quad (22)$$

Like in the previous ZVS transition period, the current dip occurs to the resonant current i_{Lr}. This is due to the current divider effect due to the output capacitance of primary and secondary switches. The resonant current i_{Lr} ringing amplitude is affected by the ratio C_{ps}/C_{oss}. High C_{ps}/C_{oss} may lead i_{Lr} to be positive, which affects the V_{ds2} decreasing rate. If C_{ps} is too large, it requires longer dead time for the resonant current i_{Lr} to discharge. This will affect the ZVS transition period at high frequency. The expression for V_{ds2} is

$$V_{ds2}(t) = V_{in} + \frac{I_{Lm\_min}t}{2C_{oss}+C_{ps}} + \frac{I_{Lm\_min}C_{ps}}{2C_{oss}+C_{ps}}\frac{1}{\omega_r 2C_{oss}}\sin(\omega_r t) \quad (23)$$

A simulation is conducted to illustrate this phenomenon. As shown in Fig.6, the blue curve with low C_{ps} is decreasing faster and turns off earlier than the red curve with high C_{ps}. In high frequency converter design, dead time control is of great importance. It is desirable to have a very short ZVS transition period to minimize the circulation power loss.

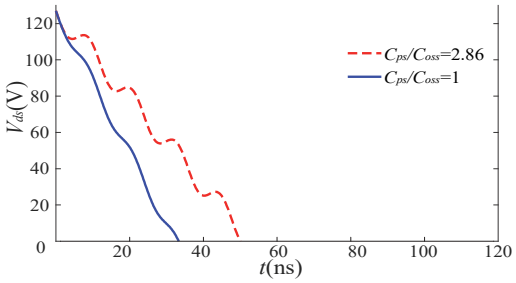

Fig.6 Drain-to-source voltage for Q_2 during ZVS transition time

Additionally, due to the small I_{Lm_min}, it takes several resonant periods to fully discharge Q_2. This can also be observed in Fig.6. On the other hand, the magnetizing current I_{Lm_max} is much larger than I_{Lm_min}. During the ZVS transition after Q_2 turns off, Q_1 is usually fully discharged within one resonant period. The decreasing rate of V_{ds1} is almost linear. Therefore, only the dead time from t_4 to t_5 is considered.

This period ends when Q_2 is fully discharged and realizes ZVS turn on. Q_1 will be clamped by the input voltage.

TABLE II
SPECIFICATION

Quantity	Range
$V_{in}(V)$	100~250
$V_o(V)$	19.3
$P_o(W)$	65
f_s	1MHz

III. Optimal Design Procedure

The specification is shown in TABLE II. Since the voltage stress for primary devices is reduced to input voltage V_{in} for the proposed topology, both switches and turns ratio selection have a larger margin than traditional ACF. In this design, the converter is designed to operate at discontinues conduction mode (DCM). The negative i_{Lm} helps ZVS

operation. The resonant inductance L_r is integrated into the transformer by using its leakage inductance. The optimal design procedure will be given in this section.

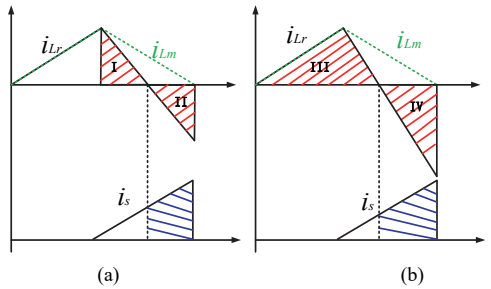

Fig.7 Comparison of ideal transformer winding current in (a) traditional ACF and (b) AHB flyback

A. Considerations of transformer power loss

Transformer power loss consists of core loss and winding loss. Core loss increases significantly at high frequency. The core material ML91S from Hitachi shows good performance at 1MHz [34] and is selected for the core material.

Flux cancellation for the traditional ACF is pointed out in [15], as shown in Fig.7 (a). The negative primary current helps the flux cancellation in the transformer and winding loss will be reduced compared to the traditional flyback converter. Actually, this is because the resonant capacitor has to satisfy the law of current-second-balance during the resonant period. The shaded area I should be exactly the same with area II as shown in Fig.7(a). On the other hand, since the resonant capacitor of the AHB flyback converter is connected in series with the transformer, the current-second-balance law is applied during the whole switching period. The shaded area III should be exactly the same with area IV as shown in Fig.7 (b). As a result, it also achieves flux cancellation and the current is also evenly distributed in the winding like traditional ACF.

B. Magnetizing inductance design

In order to achieve ZVS turn-on for Q_2, the magnetizing inductance should be designed to provide enough negative current. The ZVS realization can be described by the charge balance

$$I_{Lm\_\min} t_d = 2C_{oss}V_{in} + C_{ps}\frac{V_{in}}{n} + C_w V_{in} \tag{24}$$

where C_w is the transformer parasitic capacitance referred to the primary side. Combine (6), (18) and (24), the magnetizing inductance can be derived in (25). The optimal magnetizing inductance can be designed from the analysis of RMS current.

$$L_m = \frac{n^2 V_o (1-D)(T_s - t_d) t_d}{(4nC_{oss} + 2C_{ps} + 2nC_w)V_{in} + 2I_o t_d} \tag{25}$$

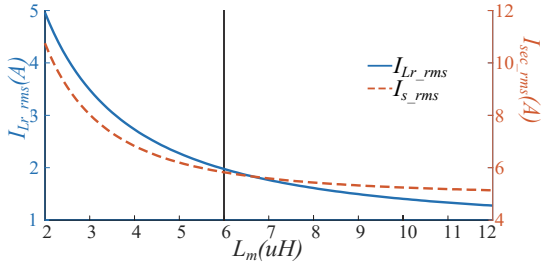

Fig.8 L_m impact on I_{Lr_rms} and I_{s_rms}

C. Primary and secondary RMS current

The RMS current should be calculated first to estimate the power loss. The definition equation of RMS is

$$I_{rms} = \sqrt{\frac{1}{T_s}\int_b^a i(t)^2\,dt} \tag{26}$$

Combine (16), (17) and (26), the RMS current on Q_1 I_{ds1_rms} can be described. Maple is used to solving the bulky equation. Similarly, combine (4) and (26), the RMS current on Q_2 I_{ds2_rms} is derived. The resonant current RMS value I_{Lr_rms} can be calculated by

$$I_{Lr\_rms} = \sqrt{I_{ds1\_rms}^{\ 2} + I_{ds2\_rms}^{\ 2}} \tag{27}$$

The secondary current i_s is the difference of the magnetizing current to resonant current from t_3 to t_4, which can be expressed by

$$i_s(t) = i_{Lm}(t) - i_{Lr}(t) \quad (t_3 < t < t_4) \tag{28}$$

Combine (5),(6),(15) to (21) and (28), the secondary RMS current I_{s_rms} is derived. The impact of magnetizing inductance on primary and secondary RMS current is summarized in Fig.8. It can be concluded that the magnetizing inductance should be maximized as possible to reduce power loss. Meanwhile, it should be smaller enough to discharge all parasitic capacitances during dead time. The optimal magnetizing inductance and corresponding dead time can then be determined from Fig.9 referring to (25).

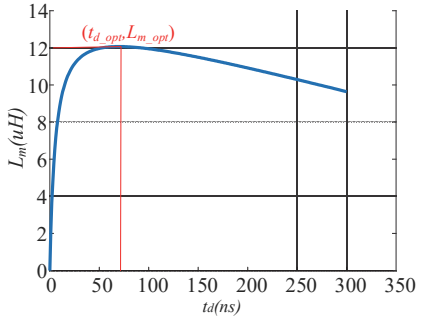

Fig.9 Magnetizing inductance versus dead time

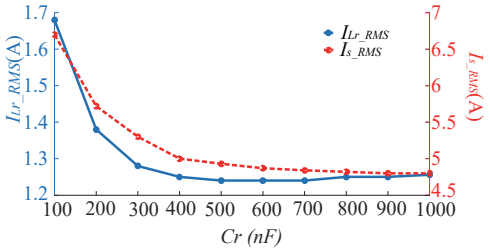

Fig.10 Resonant capacitor impact on primary and secondary RMS current

D. Resonant capacitor design

The turn-off current on auxiliary switch Q_1 and secondary rectifier is small if the resonant current i_{Lr} is close to the magnetizing current i_{Lm} at the end of resonance. In this case, a small C_r is desirable to obtain the low turn-off current through the high side Q_1 and secondary rectifier. However, both primary and secondary RMS current increase with the smaller C_r, as shown in Fig.10. On the other hand, the larger C_r means smaller RMS current while larger turn-off current on auxiliary switch Q_1 and secondary rectifier. The AHB flyback converter has significantly reduced the voltage stress on active components. Thus the turn-off loss is greatly reduced. The large C_r is desirable to minimize conduction

loss after iteration.

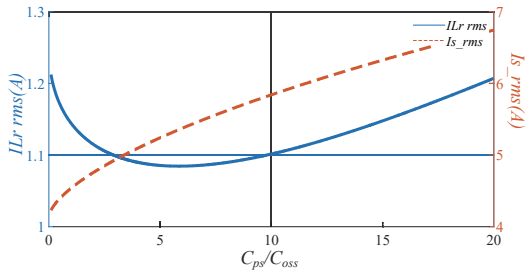

Fig.11 Primary and secondary RMS current under different C_{ps}/C_{oss} when V_{in}=127V, n:1=3:1

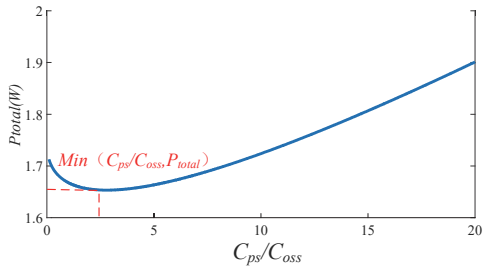

Fig.12 C_{ps}/C_{oss} impact on converter total power loss

E. Current dip effect

The impact of the current dip causing by the current divider effect of primary and secondary output capacitance is investigated and summarized in Fig.11. $2C_{oss}+C_{ps}$ is kept constant to ensure the same negative magnetizing current. Larger C_{ps}/C_{oss} contributes to higher I_{s_rms}. On the other hand, I_{Lr_rms} is decreasing to a certain value and then increasing. Therefore, the secondary SR should be selected taking into consideration the whole converter power loss. The relationship of converter total power loss P_{total} and C_{ps}/C_{oss} is shown in Fig.12. C_{ps}/C_{oss} between 2 and 4 achieves minimal loss. This can be used to select primary and secondary switches. Given that switches of specific characteristics change slightly in different devices of the same part number, the primary and secondary switches are selected referring to information in the datasheet.

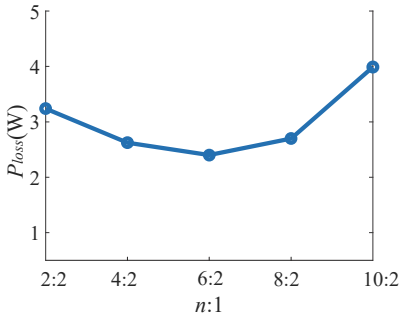

Fig.13 Total power loss under different turns ratio

F. Turns ratio selection

The turns ratio selection is of great importance to design a high efficiency converter. It has several impacts on the converter design. For ACF converters, both primary and secondary switches selections are relating to the turns ratio, as shown in TABLE I. However, for the AHB flyback converter, the voltage stress for the primary switches is V_{in}, which has no relation with the turns ratio. Moreover, the turns ratio selection also affects both primary and secondary RMS current [15] and transformer core loss. In other words, the converter total power loss is affected by the turns ratio. An iteration is needed for the optimal design.

TABLE III
CIRCUIT PARAMETERS

Circuit parameters	Value
Primary devices	GS66502B
Secondary rectifier	EPC2033
Magnetizing inductance L_m	11uH
Resonant inductance L_r	195nH
Resonant capacitance C_r	430nF
Magnetic core	EI22/6/16-ML91S
Turns ratio	6:2

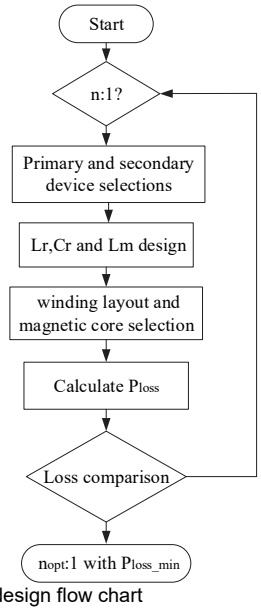

Fig.14 Optimal design flow chart

Based on the design procedure as mentioned above, a flow chart is made to obtain the optimal design, as shown in Fig.14. Iterations for the optimal turns ratio selection are performed and the corresponding power loss when V_{in}=100V is shown in Fig.13. 6:2 yields the minimum power loss and is determined for the transformer design. Finally, the circuit parameters are listed in TABLE III. GaN devices 650V GS66502B from GaN system are selected for primary switches due to the lower output capacitance compared to 350V EPC2050. GaN devices with lower voltage ratings, for example, 300V, can be selected when they are available in the market. EPC2033 is used for secondary SR. The ratio of C_{ps}/C_{oss} is 2.87.

To operate at MHz frequency, planar transformers illustrate better performance than conventional transformers [26]-[32]. Secondary windings are connected in parallel to further reduce winding loss. A half-turn paralleled winding practice is first proposed in [26]. The paralleled winding structure along with the magnetomotive force (MMF) distribution is shown in Fig.15. The number of layers m_p for primary windings and m_s for secondary windings can be derived from the MMF distribution, which is 0.5 and 1, respectively. The current distribution conducted by 2-D FEA simulation at 1 MHz shown in Fig.16. Air gaps are created on all three legs of the magnetic core E22/6/16. The current distribution for secondary windings S1_1 located on the top and S2_2 located on the bottom are identical, while they are a little bit lower than the current distribution for S1_2 and S2_1 in the middle having the same current distribution. The secondary current can be taken as uniformly distributed in this paralleled winding structure. Thus this winding structure contributes to a low AC winding loss.

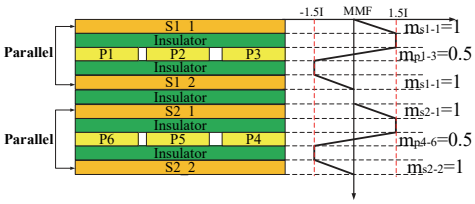

Fig.15 Half-turn paralleled winding structure and MMF distribution

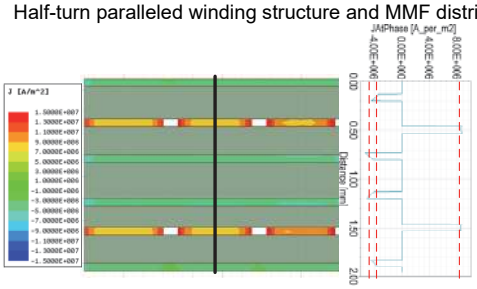

Fig.16 Current density distribution conducted by 2-D FEA simulation at 1 MHz

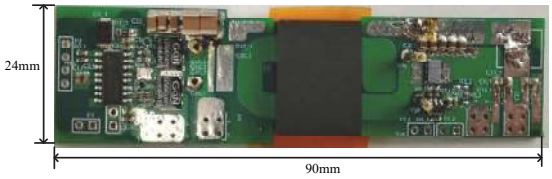

Fig.17 1MHz 65W prototype with 56W/inch^3 power density

IV. Experiment Verification

A 1MHz, 65W, 19.3V prototype is built to verify the feasibility of the converter, as shown in Fig.17. GaN devices are used for both primary and secondary switches. Fig.18 shows the measured drain-to-source voltage waveform of Q_2 and the resonant current waveform when input DC voltage is 127V. ZVS for Q_2 is achieved despite the deceasing rate is affected by the resonance that happens to i_{Lr}. As discussed in Section II, i_{Lr} ringing amplitude is affected by C_{ps}/C_{oss}. High C_{ps}/C_{oss} may lead i_{Lr} to be positive, which affects the V_{ds1} decreasing rate. The current dip effect during ZVS transition time can be easily observed from Fig.18 (b) with an external 330pF film capacitor connected in parallel with the secondary rectifier. The ZVS transition time becomes obviously longer than the converter without external C_{sj}. This proves the effectiveness of previous analysis in Section II.

Efficiency curves under whole input voltage range at full load condition are shown in Fig.19. The output current I_o was measured by the multi-meter Keysight 34465A. The output voltage V_o, input voltage V_{in} and input current I_{in} are measured by three multimeters Agilent 34410A, respectively. The 96.5% peak efficiency is achieved when the input voltage is 127V for the converter without external C_{sj}. The total system efficiency is above 93% under the whole input voltage range.

The Efficiency curves comparison with the converter built in [23] is given in Fig.19. The converter presented in this paper is almost higher than the others under the whole input voltage range. Loss break down at 127V is shown in Fig.20.Winding loss and conduction loss dominates. The detailed comparison shown in TABLE IV proves the effectiveness of the optimal design procedure given in Chapter III. The peak efficiency of converters built in [35] and [36] is 96.4% and 96.25%, respectively. However, these converters are operating at a low frequency around 200 kHz. Switching frequency affects the converter total power loss in several aspects. High switching frequency contributes to high AC resistance, high switching loss (turn-off loss in this case) and high core loss, but it improves the power density. The switching frequency in this paper is 1MHz, but comparable efficiency is still achieved. Those operating at 1MHz are illustrated in [37] and [33] and the peak efficiency for these converters are 90.1% and 93%, respectively. Hence, the proposed AHB flyback converter is quite competitive.

The uncertainty analysis is done to justify the measured peak efficiency. Type A, Type B and combined standard uncertainty are summarized in TABLE V. It should be noted here that the confidence level is not given in datasheet of the measurement. 95% confidence level is assumed and the coverage factor is selected to be 2.

The built prototype verifies the effectiveness of the optimal design procedure. It benefits from the better high frequency performance core material and interleaved winding layout. Taking the impact of the current dip effect into consideration, primary and secondary switches are selected to minimize the power loss. Together with the optimal design of magnetizing inductance, resonant capacitor and turn ratio selection, a high performance converter is built.

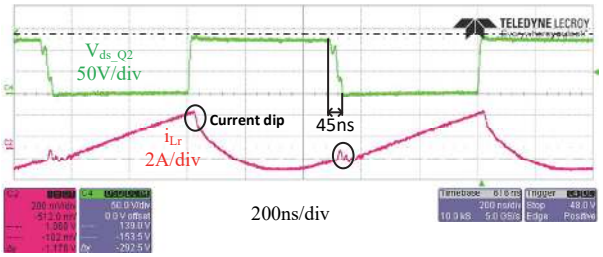

(a)

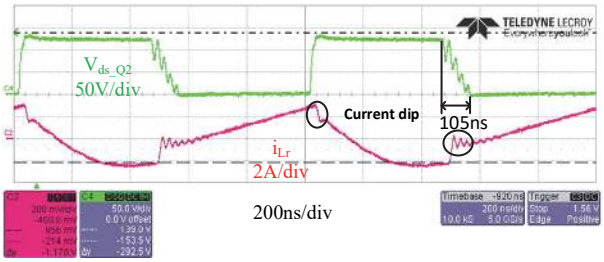

(b)

Fig.18 Experimental waveforms tested at 127V$_{ds}$: (a) without external C$_{sj}$ (b) with 330pF external C$_{sj}$

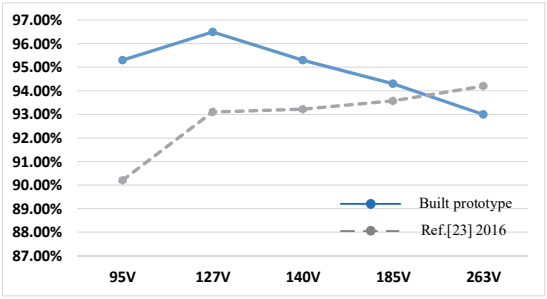

Fig.19 Efficiency curves measured at full load conditions

TABLE IV
Efficiency Comparison

	Frequency	Efficiency
Ref.[35]	200kHz	96.40%
Ref.[36]	200kHz	96.25%
Ref.[37]	1MHz	90.10%
Ref.[33]	1MHz	93%
This paper	1MHz	96.50%

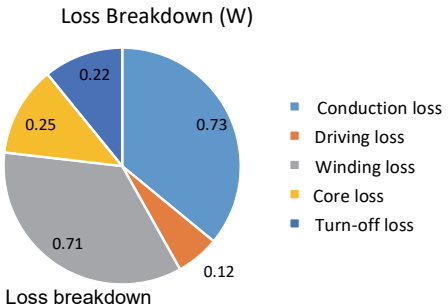

Fig.20 Loss breakdown

TABLE V
UNCERTAINTY ANALYSIS

Type		V_{in}(V)	I_{in}(A)	V_o(V)	I_o(A)
A	AVG.	126.75	0.5327	19.339	3.37
	SDEV.	0.625	0.0034	0.0514	0.0109
	DOF.	4	4	4	4
B	u_i	0.01	0.00025	0.001	0.0025
Combined	u_i	0.6246	0.0034	0.0514	0.0111

V. Conclusion

This paper gives detailed analyses of the AHB flyback converter. It can be regarded as a buck converter with a transformer. Thus this converter is well adapted to voltage step-down applications. Larger margin is given for components selection and turns ratio design. GaN devices with lower voltage ratings, for example, 300V, can be selected for primary switches when they are available in the market.

The detailed analysis of the circuit is presented, including both steady-state and transient analyses. The current divider effect affects primary and secondary RMS current. This can be used to select primary and secondary switches. At Mega Hz operation, the dead time is of great importance to design magnetizing inductance. The optimal magnetizing inductance design with the consideration of dead time is investigated. The design procedure, including the resonant capacitor, primary and secondary switches selection and turns ratio design contributes to a high efficiency AHB flyback converter.

Finally, a 56W/inch^3 1MHz 65W prototype is built to verify the feasibility of the proposed converter. It achieves 96.5% peak efficiency at 127V. The whole system efficiency under the entire input voltage range is above 93%.

References

[1] Z. Zhang, J. Y. Lin, Y. Zhou and X. Ren, "Analysis and decoupling design of a 30 MHz resonant SEPIC converter," IEEE Trans. Power Electron., vol. 31, no. 6, pp. 4536-4548, Jun. 2016.

[2] Z. Zhang, Z. Dong, D. D. Hu, X. W. Zou, and X. Ren, "Three-level gate drivers for eGaN HEMTs in resonant SEPIC converters," IEEE Trans. Power Electron., vol. 32, no. 7, pp. 5527–5538, Jul. 2017.

[3] X. Huang, Z, Liu, F. C. Lee, and Q. Li, "Characterization and enhancement of high-votlage cascode GaN devices," IEEE Trans. on Electron Devices, vol. 62, no. 2, pp.270-277, Feb. 2015.

[4] X. Huang, W. Du, F. C. Lee, and Q. Li, "A novel driving scheme for synchronous rectifier in MHz CRM flyback converter with GaN devices, " in proc. IEEE ECCE, 2015, pp 5089-5095.

[5] Z. Zhang, K. D. T. Ngo, and J. L. Nilles, "A 30-W flyback converter operating at 5 MHz," in proc.IEEE APEC, 2014, pp 1415-1421.

[6] C. T. Choi, C. K. Li and S. K. Kok, "Modeling of an active clamp discontinuous conduction mode flyback converter under variation of operating conditions", IEEE-PEDS, vol. 2, pp. 730- 733, 1999.

[7] R. Watson, F. C. Lee, and G. C. Hua, "Utilization of an active clamp circuit to achieve soft-switching in flyback converters", IEEE Transactions on Power Electronic, vol. 11, no. 1, pp. 162-169, 1996.

[8] Y.-S. Lee and B.-T. Lin, "Adding Active Clamping and Soft-switching to Boost-Flyback Single-Stage Isolated Powersource voltage for main switch. Factor-Corrected Power Supplies", IEEE Transactions on Power Electronics, vol. 12, no. 6, pp. 1017-1027, 1997.

[9] J. J. Lee, J. M. Kwon, E. H. Kim, and B. H. Kwon, "Dual series-resonant active-clamp converter," IEEE Trans. Ind. Electron., vol. 55, no. 2, pp. 699–710, Feb. 2008.

[10] Spiazzi, G., Mattavelli, P., & Costabeber, A. " High Step-Up Ratio Flyback Converter With Active Clamp and Voltage Multiplier". IEEE Transactions on Power Electronics, vol. 26, no.11, pp.3205-3214. 2011.

[11] J. Zhang, X. Huang, X. Wu, Z. Qian, "A High Efficiency Flyback Converter With New Active Clamp Technique", IEEE Transactions on Power Electronics, vol. 25, n. 7, 2010, pp. 1775-1785

[12] N. P. Papanikolaou, and E. C. Tatakis, "Active Voltage Clamp in Flyback Converters Operating in CCM Mode Under Wide Load Variation," IEEE Transactions on Industrial Electronics, vol. 51, no. 3, pp.632-640, June 2004

[13] Hadi Tarzamni, Ebrahim Babaei, Amirreza Zarrin Gharehkoushan, "A Full Soft-Switching ZVZCS Flyback Converter Using an Active Auxiliary Cell", IEEE Transactions on Industrial Electronics, vol. 64, no. 2, pp. 1123-1129, 2017

[14] Xue, Lingxiao, and Jason Zhang. "Highly Efficient Secondary-Resonant Active Clamp Flyback Converter." IEEE Transactions on Industrial Electronics, vol. 65, no. 2, 2018, pp. 1235–1243

[15] Xiucheng Huang, Junjie Feng, Weijing Du, Fred C. Lee, Qiang Li, "Design consideration of MHz active clamp flyback converter with GaN devices for low power adapter application", Applied Power Electronics Conference and Exposition (APEC) 2016 IEEE, pp. 2334-2341, 2016.

[16] S. R. Bahl, D. Ruiz, and D. S. Lee, "Product-level Reliability of GaN Devices," IEEE International Reliability Physics Symposium, pp. 4A-3- 1~4A-3-6, 2016.

[17] R. Hou, J. Xu, and D. Chen, "A multivariable turn-on/turn-off switching loss scaling approach for high-voltage GaN HEMTs in a hard-switching half-bridge configuration," in IEEE Workshop on Wide Bandgap Power Devices and Applications (WiPDA), Oct 2017, pp. 171–176.

[18] T.Chen and C. Chen, "Analysis and design of asymmetrical half bridge flyback converter," in IEEE Proceedings - Electric Power Applications, vol. 149, no. 6, pp. 433-440, Nov. 2002.

[19] H. Kim, J. Jung, J. Baek, and H. Kim, "Analysis and Design of a Multi-output Converter using Asymmetrical PWM Half-bridge Flyback Converter Employing a Parallel-series Transformer," IEEE Transactions on Industrial Electronics, pp. 1–1, 2012.

[20] Jee-Hoon Jung, "Feed-Forward Compensator of Operating Frequency for APWM HB Flyback Converter," IEEE Trans. on Pow Electron, vol. 27, no. 1, pp. 211-223, 2012

[21] H. Kim, J. Jung, J. Baek, and H. Kim, "Analysis and Design of a Multi-output Converter using Asymmetrical PWM Half-bridge Flyback Converter Employing a Parallel-series Transformer," IEEE Transactions on Industrial Electronics, pp. 1–1, 2012.

[22] Han Li, Wenjun Zhou, Shiping Zhou, Xiao Yi, "Analysis and Design of High Frequency Asymmetrical Half Bridge Flyback Converter", International Conference on Electrical Machines and Systems, 2008, p.1902-1904.

[23] Chen, Yu-Fu, et al. "Hybrid-Switching Asymmetrical Half-Bridge Flyback DC-DC Converter." 2016 IEEE International Conference on Industrial Technology (ICIT), 2016.

[24] Laszlo Huber ; Milan M. Jovanović. "Analysis, Design, and Performance Evaluation of Asymmetrical Half-Bridge Flyback Converter for Universal-Line-Voltage-Range Applications." Applied Power Electronics Conference and Exposition (APEC) 2017 IEEE, 2017.

[25] G. Y. Jeong, "High efficiency asymmetrical half-bridge flyback converter using a new voltage-driven synchronous rectifier," in IET Power Electronics, vol. 3, no. 1, pp. 18-32, January 2010.

[26] Z. Ouyang and M. Andersen, "Overview of planar magnetic technology; fundamental properties," IEEE Trans. on Pow Electron, vol. 29, no. 9, pp. 4888-4900, Sep. 2014

[27] Z. Ouyang, O. C. Thomsen, and M. A. E. Andersen, "Optimal design and tradeoff analysis of planar transformer in high-power DC–DC converters," IEEE Trans. Ind. Electron., vol. 59, no. 7, pp. 2800-2810, Jul. 2012.

[28] Zhang, Zhiliang, et al. "Multi-Winding Configuration Optimization of Multi-Output Planar Transformers in GaN Active Forward Converters for Satellite Applications." IEEE Transactions on Power

Electronics, vol. 34, no. 5, 2019, pp. 4465-4479.
[29] M. Li, Z. Ouyang and M. A. E. Andersen, “High frequency LLC resonant converter with magnetic shunt integrated planar transformer,” IEEE Trans. Power Electron, 2018.
[30] M. A. Saket, N. Shafiei and M. Ordonez, “LLC Converters with planar transformers: issues and mitigation," IEEE Trans. Power Electron., vol. 32, no. 6, pp. 4524-4542, Jun. 2017.
[31] X. Liu, R. Burgos, B. Sun, and D. Boroyevich, “Wide-input-voltagerange dual-output GaN-based isolated DC-DC converter for aerospace applications,” in Proc. IEEE Appl. Power Electron. Conf. Expo., Tampa, FL, USA, 2017, pp. 279–286.
[32] B. Sun, R. Burgos and D. Boroyevich, "Ultra-low Input-Output Capacitance PCB-Embedded Dual-Output Gate-Drive Power Supply for 650 V GaN-Based Half-Bridges," in IEEE Transactions on Power Electronics.
[33] Liu, Yu-Chen, et al. “Design and Implementation of a High Power Density Active-Clamped Flyback Converter.” International Power Electronics Conference (IPEC) 2018, IEEE, pp.2092-2096
[34] C. Fei, F. C. Lee, and Q. Li, “High-efficiency high-power-density LLC converter with an integrated planar matrix transformer for high output current applications,” IEEE Trans. Ind. Electron., vol. 64, no. 11, pp. 9072–9082, Nov. 2017.
[35] L. Huber, M. M. Jovanovic, H. Song, D. Xu, A. Zhang, and C.-C. Chang, “Flyback converter with hybrid clamp,” 2018 IEEE Applied Power Electronics Conference and Exposition (APEC), 2018.
[36] H. Song, D. Xu, and A. J. Zhang, “Comparison between Control Methods of Active Clamp Flyback for Adaptor Application,” 2018 IEEE International Power Electronics and Application Conference and Exposition (PEAC), 2018.
[37] F.-C. Syu, S.-C. Yeh, Y.-C. Chang, J.-Y. Lin, Y.-C. Hsieh, H.-J. Chiu, M. Hojo, and K. Yamanaka, “Design and implementation of 1 MHz active-clamped resonant flyback converter,” IECON 2017 - 43rd Annual Conference of the IEEE Industrial Electronics Society, 2017.

Mingxiao Li received the B.S degree in electrical engineering from Chongqing University, Chongqing, China, in 2016 and M.S. degree in electrical engineering in 2018 from Technical University of Denmark, Kongens Lyngby, Denmark, where he is currently working toward the Ph.D degree in electrical engineering.
His research interests include magnetics design, modeling and integration in power supplies, resonant converters and high frequency power conversion.

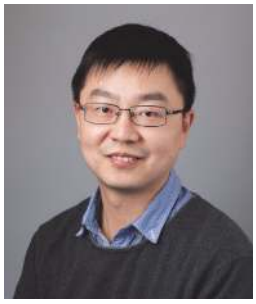

Ziwei Ouyang (S’07, M’11, SM’17) received the Ph.D. degree from the Technical University of Denmark (DTU), Kgs. Lyngby, Denmark, in 2011. From 2011 to 2013, he was a Postdoc Researcher with DTU. From 2013 to 2016, he was appointed as an Assistant Professor at DTU. Since April 2016, he has been an Associate Professor with DTU. His research areas focus on high-frequency planar magnetics modeling and integration, high-density high-efficiency power converters, PV battery energy storage system, and wireless charging etc. He is currently responsible for the Power Electronics course for both undergraduate and graduate students at DTU, and he also supervised more than 40 students’ Postdoc, Ph.D., and Masters projects. He has more than 60 high impact IEEE journal and conference publications, and has coauthored a book chapter on Magnetics for the Handbook of Power Electronics and currently is the holder of 8 international patents.
Dr. Ouyang was the recipient of the Young Engineer Award at PCIM-Asia 2014, and the Best Ph.D. Dissertation of the Year Award 2012 in Technical University of Denmark, and several Best Paper Awards in IEEE sponsored international conferences. He has served as the session Chair in some IEEE sponsored conferences and a Reviewer for the IEEE TRANSACTIONS ON POWER ELECTRONICS and IEEE TRANSACTIONS ON INDUSTRIAL ELECTRONICS.

Michael A.E. Andersen (M’88) received the M.Sc.E.E. and Ph.D. degrees in power electronics from the Technical University of Denmark, Kgs. Lyngby, Denmark, in 1987 and 1990, respectively. He is currently a Professor of power electronics at the Technical University of Denmark, where since 2009, he has been the Deputy Head of the Department of Electrical Engineering. He is the author or coauthor of more than 300 publications. His research interests include switch-mode power supplies, piezoelectric transformers, power factor correction, and switch-mode audio power amplifiers.